LES And URANS simulations of the swirling flow in a dynamic model of a uniflow-scavenged cylinder

Casper S. Hemmingsen [a,*], Kristian M. Ingvorsen [a], Stefan Mayer [b], Jens H. Walther [a,c]

[a] Department of Mechanical Engineering, Technical University of Denmark, Building 403, DK-2800 Kgs. Lyngby, Denmark
[b] MAN Diesel & Turbo SE, Teglholmsgade 41, DK-2450, Copenhagen SW
[c] Computational Science and Engineering Laboratory, ETH Zürich, Clausiusstrasse 33, CH-8092 Zürich, Switzerland

ARTICLE INFO

ABSTRACT

The turbulent swirling flow in a uniflow-scavenged two-stroke engine cylinder is investigated using computational fluid dynamics. The investigation is based on the flow in a scale model with a moving piston. Two numerical approaches are tested; a large eddy simulation (LES) approach with the wall-adaptive local eddy-viscosity (WALE) model and a Reynolds-Averaged Navier-Stokes approach using the $k - \omega$ Shear-Stress Transport model. Combustion and compression are neglected. The simulations are verified by a sensitivity study and the performance of the turbulence models are evaluated by comparison with experimental results. Both turbulence models produce results in good agreement with experimental data. The agreement is particularly good for the LES, immediately after the piston passes the bottom dead center. Furthermore, in the piston standstill period, the LES predicts a tangential profile in agreement with the measurements, whereas the $k - \omega$ SST model predicts a solid body rotation. Several instabilities are identified during the scavenging process. The formation of a vortex breakdown with multiple helical vortex structures are observed after the scavenge port opening, along with the shedding of vortex rings with superimposed swirl. The turbulence models predict several flow reversals in the vortex breakdown region through the scavenge process. Flow separations in the scavenge ports lead to a secondary axial flow, in the separated region. The secondary flow exits in the top of the scavenge ports, resulting in large velocity gradients near the cylinder liner above the scavenge ports.

© 2016 Elsevier Inc. All rights reserved.

1. Introduction

The de-facto standard propulsion technology for bulk carriers, tankers and container vessels is that of the marine low-speed two-stroke uniflow-scavenged diesel engines. The gas exchange process, the so called scavenging process, is an important part of the engine process. The scavenging of the cylinder ensures delivery of fresh air to the combustion process, removes combustion gases in the cylinder, cools the combustion chamber surfaces, and distributes fuel in the combustion chamber. The efficiency of the scavenging process is therefore crucial for the total engine efficiency.

When the piston approaches the bottom dead center (BDC), it uncovers a series of angled scavenge ports. Fresh air is blown into the cylinder thereby removing the old combustion gases through the exhaust valve in the cylinder cover. The common practice of the uniflow scavenging process is to inject the fresh air with a tangential component into the cylinder, thereby creating a swirling flow. The strength of the swirl is, to a large extend, controlled by the angle and design of the scavenge ports.

Simulations of turbulent flow is usually performed using unsteady Reynolds-Averaged Navier–Stokes (URANS) based methods, but they are known to be inaccurate for the description of highly rotating flows (Hoekstra et al., 1999; Najafi et al., 2005; Yuan and So, 1998). Reliable knowledge of the modelling accuracy for the swirling flow, is important for using the numerical models for design purposes.

Experimental investigations of the in-cylinder flow is mainly limited to scale models, due to the size and hostile running environment of full two-stroke diesel engines. Experimental investigations include measurements under steady-flow conditions (Haider et al., 2013; Ingvorsen et al., 2013; Percival, 1955; Sung and Patterson, 1982) and measurement under dynamic conditions (Ingvorsen et al., 2014; Nakagawa et al., 1990). Numerical investigations of the swirling in-cylinder flow includes 2D-axisymmetric simulations (de Castro Gouveia et al., 1992; Diwakar, 1987; Ravi and Marathe, 1992; Sher et al., 1991; Sung and Patterson, 1982; Uzkan, 1988), sector simulations (Carapanayotis, 1988; Sigurdsson et al., 2014)

* Corresponding author.
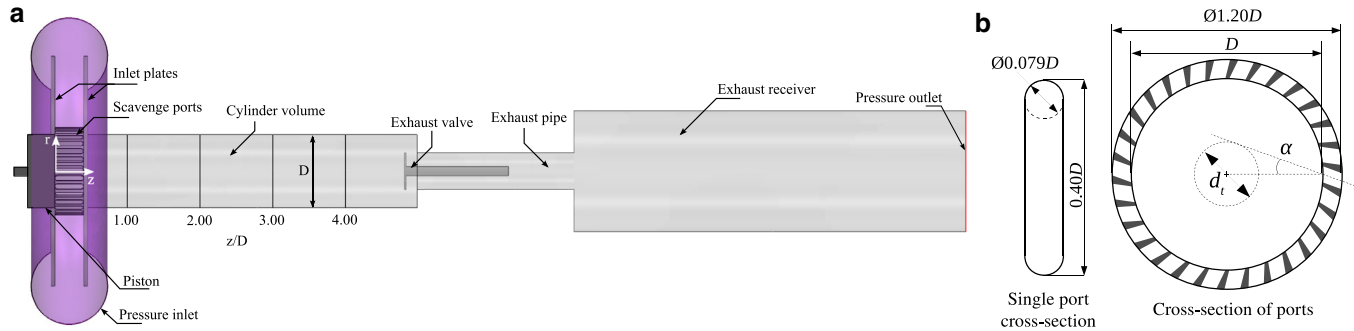 *E-mail address:* casche@mek.dtu.dk (C.S. Hemmingsen).

Fig. 1. a) Schematic of the model engine b) Geometric details of the scavenge ports.

and full three-dimensional (3D) simulations (Al-Mousawi, 2012; Goldsborough and Blarigan, 2003; Hori, 2000; Lamas and Vidal, 2012; Obeidat et al., 2014). The full 3D simulations are, in general, carried out using low spatial and temporal resolution, and with grid independence studies on fast converging parameters. The majority of the numerical simulations are carried out using different variations of the $k - \epsilon$ turbulence model, however the preliminary study of Al-Mousawi (2012) found that URANS models are poor at reproducing the swirling flow in a steady-flow configuration. Instead the study shows a good agreement between experimental data and the large-eddy simulations (LES) using the wall-adaptive local eddy-viscosity (WALE) subgrid-scale model (Al-Mousawi, 2012).

In the present work full 3D computational fluid dynamic (CFD) simulations of a scale model of the MAN Diesel & Turbo 4T50ME-X research engine (Hult and Mayer, 2013) are performed. The engine is a large two-stroke low-speed uniflow-scavenged marine diesel engine with a bore size of 0.5 m. The Reynolds number of the engine is $Re = 2,600,000$ (Ingvorsen et al., 2013). Detailed simulations of the flow are performed, including verification of convergence in terms of spatial and temporal scales. Different turbulence models are validated against the experimental database presented by Ingvorsen et al. (2014).

2. Methodology

2.1. Experimental benchmark

The configuration considered in the present study is the experimental set-up of Ingvorsen et al. (2014) of a simplified scale model of the 4T50ME-X test engine.

Flow measurements inside the cylinder were carried out with stereoscopic particle image velocimetry (PIV) and laser Doppler anemometry (LDA), using a glass cylinder with good optical properties. Fig. 1 illustrates the geometry of the set-up. The inner diameter of the cylinder is $D = 190$ mm and the cylinder length is 5.00D. The scavenging ports consist of $n_p = 30$ equally spaced ports angled $\alpha = 20°$ (cf. Fig. 1b). The port height is 0.40D and the width is 0.079D, with rounded top and bottom. At the cylinder head, an exhaust pipe is attached with internal diameter 0.50D and length 2.16D. A fixed exhaust valve is placed inside the exhaust pipe. The exhaust valve consist of a disc (diameter 0.50D, thickness 0.02D) placed on a circular rod (diameter 0.126D, length 1.34D). The exhaust pipe ends in the exhaust receiver with diameter 1.66D and length 5.40D.

The Reynolds number based on the scavenge velocity is $Re_{sc} = U_{sc}D\nu^{-1} = 50,000$, where ν is the kinematic viscosity, and U_{sc} is the scavenge velocity. The scavenge velocity is defined as $U_{sc} = m_{sc}(\rho t_{sc} A_{cyl})^{-1}$, where m_{sc} is the mass of scavenged gas per cycle, t_{sc} is the scavenge period (port open period), A_{cyl} is the cross-sectional area of the cylinder, and ρ is the fluid density. Using the
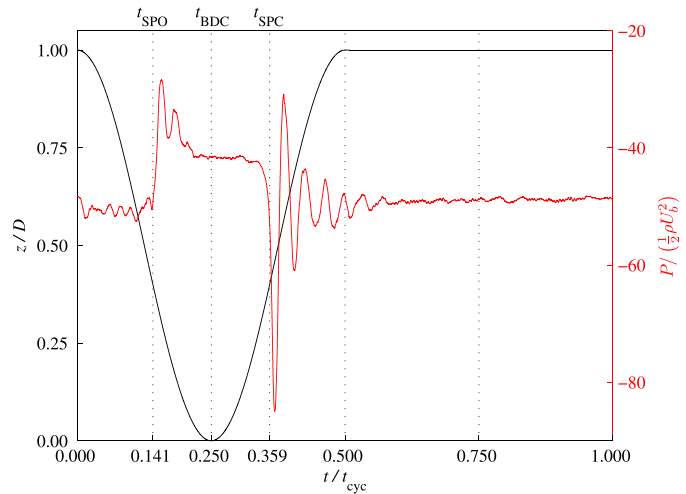

Fig. 2. Piston motion, sinusoidal movement between $0.000t_{cyc} - 0.500t_{cyc}$ and standstill for the remaining cycle (*black line*). Experimental pressure measurements Ingvorsen et al. (2014) measured at the outlet of the exhaust receiver (*red line*). The scavenging process takes place between scavenge ports open (SPO) and scavenge ports close (SPC). (For interpretation of the references to colour in this figure legend, the reader is referred to the web version of this article.)

fixed bulk velocity, U_b, as reference velocity the Reynolds number is $Re_b = 60,000$. The bulk velocity U_b is experimentally obtained with PIV at $z/D = 1.5$ based on the radial profile of the axial velocity when the piston is at BDC. The piston motion follows a sinusoidal motion for $t_{cyc}/2$, and for the remaining cycle time it is fixed at $z/D = 1.00$ (cf. Fig. 2). The scavenge ports open (SPO) at $t/t_{cyc} = 0.141$, initializing the scavenge process. The piston reaches the bottom dead center at $t/t_{cyc} = 0.250$, corresponding to fully open ports. In the remainder of this paper, the bulk velocity is determined for the individual turbulence model and used for normalization purposes. The scavenge ports close (SPC) at $t/t_{cyc} = 0.359$ and the scavenge process ends. The piston returns to 1.00D above BDC for the standstill period, before the cycle is repeated. A single cycle time is $t_{cyc} = 1.2$ s.

Pressure measurements are performed with a wall pressure tab located at the outlet of the exhaust receiver. In Fig. 2 the cyclic movement and the standstill period of the piston is shown along with the experimental cyclic averaged pressure measurements. Radial profiles of the phase averaged velocity is reported for four axial locations $z/D = \{1.00, 2.00, 3.00, 4.00\}$.

2.2. Governing equations

The flow in the simulation is assumed isothermal, and the fluid is compressible due to travelling pressure waves. The decomposed Reynolds averaged mean continuity and momentum equations for

a Newtonian fluid can be expressed, using Einstein summation and Cartesian coordinates, in conservative form (Wilcox, 1994) by

$$\frac{\partial \bar{\rho}}{\partial t} + \frac{\partial}{\partial x_j}\left(\bar{\rho}\tilde{u}_j\right) = 0 \tag{1}$$

$$\frac{\partial (\bar{\rho}\tilde{u}_i)}{\partial t} + \frac{\partial}{\partial x_j}\left(\bar{\rho}\tilde{u}_j\tilde{u}_i\right) = -\frac{\partial p}{\partial x_i} + \frac{\partial \tau_{ji}}{\partial x_j} \tag{2}$$

where x_i is the spatial coordinate, $\tilde{u}_i$ is the density-weighted velocity, p is the pressure, $\bar{\rho}$ is the Reynolds averaged density, and τ_{ji} is the stress tensor. The tilde denotes a density-weighted variable and the overbar denotes a Reynolds averaged mean. Using the Boussinesq approximation, the stress tensor is defined as

$$\tau_{ij} \approx 2\tilde{\mu}_{eff}\left(\frac{1}{2}\left(\frac{\partial \tilde{u}_i}{\partial x_j} + \frac{\partial \tilde{u}_j}{\partial x_i}\right) - \frac{1}{3}\frac{\partial \tilde{u}_k}{\partial x_k}\delta_{ij}\right) \tag{3}$$

where δ_{ij} is the Kronecker delta, the effective viscosity is defined as $\tilde{\mu}_{eff} = \tilde{\mu}_t + \tilde{\mu}$, where $\tilde{\mu}_t$ is the turbulent viscosity and $\tilde{\mu}$ is the molecular viscosity. As for the incompressible case the τ_{ij} is a symmetric tensor.

In the present work one linear eddy viscosity model is used to close the equations. The model is the two-equation $k - \omega$ Shear-Stress Transport (SST) model (Menter, 1994), using a Kármán constant of $\kappa = 0.41$.

Also a LES model is investigated using the WALE subgrid-scale model (Nicoud and Ducros, 1999). The mixing-length formula for the subgrid scale viscosity is defined as

$$\tilde{\mu}_t = \rho \Delta^2 S_w \tag{4}$$

where the filter width is defined as

$$\Delta = \mathbf{min}(\kappa d, C_w V^{1/3}) \tag{5}$$

where d is the distance to the nearest wall, C_w is a coefficient of 0.544, and V is the volume of the cell. The deformation parameter is defined as

$$S_w = \frac{\left(S_{ij}^d S_{ij}^d\right)^{3/2}}{\left(\bar{S}_{ij}\bar{S}_{ij}\right)^{5/2} + \left(S_{ij}^d S_{ij}^d\right)^{5/4}} \tag{6}$$

where

$$S_{ij}^d = \bar{S}_{ik}\bar{S}_{kj} + \bar{\Omega}_{ik}\bar{\Omega}_{kj} - \frac{1}{3}\delta_{ij}\left[\bar{S}_{mn}\bar{S}_{mn} - \bar{\Omega}_{mn}\bar{\Omega}_{mn}\right] \tag{7}$$

using the deformation tensor defined as

$$\bar{S}_{ij} = \frac{1}{2}\left(\frac{\partial \bar{u}_i}{\partial x_j} + \frac{\partial \bar{u}_j}{\partial x_i}\right) \tag{8}$$

and

$$\bar{\Omega}_{ij} = \frac{1}{2}\left(\frac{\partial \bar{u}_i}{\partial x_j} - \frac{\partial \bar{u}_j}{\partial x_i}\right) \tag{9}$$

2.3. Computational domain

The computational domain consists of an inlet section, scavenge ports region, cylinder, exhaust pipe and exhaust receiver, cf. Fig. 1. The gap between the piston and the wall, due to the presence of piston rings, is neglected assuming a small influence. The consequence of the simplification is a minor difference on the effective opening and closing time of the scavenge ports. The six rods used for mounting the valve are neglected in the numerical model. This approximation is judged acceptable since the main flow resistance is located at the valve, and only small influences on the flow resistance is expected. Also the velocity measurements are only performed in the cylinder region alone, and no effect is expected on the non-dimensional velocity field in the cylinder.

2.3.1. Boundary condition

To ensure comparable inlet conditions, the inlet boundary is applied on a toroidal shape covering the entrance upstream to the
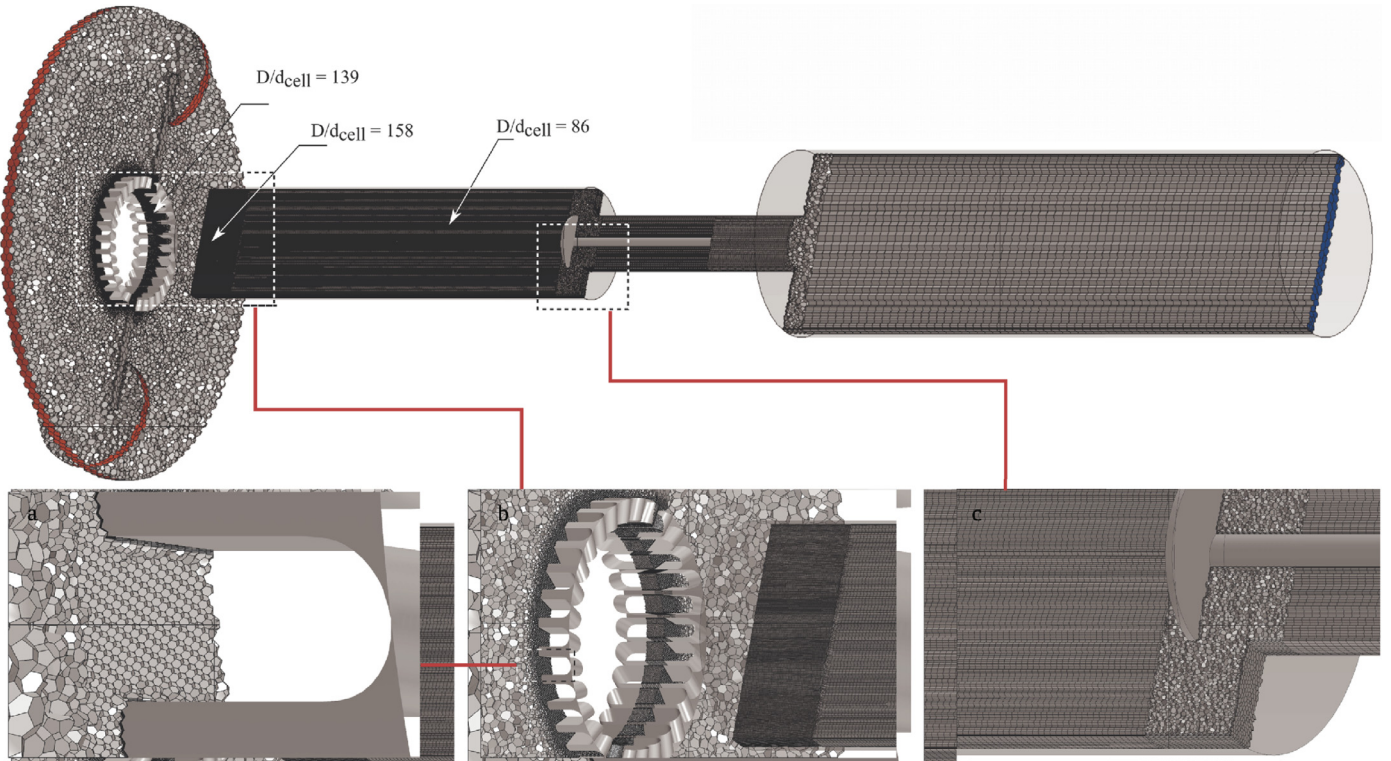

Fig. 3. Visualizations of the computational mesh with magnifications of a) a single port, b) all the ports and the lowest part of the scavenge volume, and c) the outlet valve.

inlet plates, illustrated in Fig. 1. On the inlet boundary a constant pressure boundary are applied, using the total pressure. No turbulence is applied on the toroidal shape in order to represent the experimental set-up in the laboratory environment. At the outlet of the exhaust receiver a uniform pressure boundary is applied. The outlet pressure is the cycle averaged pressure measurement shown in Fig. 2. As the cylinder wall comes in contact with the inlet ports, an internal interface is connecting the two fluid regions. All remaining boundaries are walls and a no-slip condition is applied. Two different computational domain approaches are tested, a full 3D domain and a 12° sector domain of a single port. The sector domain is investigated to reduce the size of the computational mesh, and thereby save computational time. For the sector model a periodic interface is used on the boundaries in the tangential direction.

2.4. Mesh generation

A mesh generation strategy based on polyhedral finite volumes are used to discretize the computational domain. A finite volume technique with polyhedral cells are flexible and good for complex geometries. Furthermore, the method provides good conservation of kinetic energy, especially important for the LES model (Moulinec et al., 2005). To increase the resolution in the boundary layer, prismatic cells are applied in the near-wall regions. The mesh is visualized in Fig. 3, with a total number of cells of 5.1 million. Preliminary investigations show that local refinements in the ports and the lower part of the cylinder are important to capture the high velocity gradients in these regions. The refinement in the lower region of the cylinder extends from the piston head and 0.40D downstream. The cells in this region are extruded downstream of the piston head from a 2D mesh, generated on the surface of the piston head. The ratio between the cylinder diameter and a characteristics size of the polyhedral cells on the piston head surface is $D/d_{cell} = 158$, and the ratio in the axial direction $D/z_{cell} = 163$, where z_{cell} is defined as the extruded length of the polyhedral cell surface. Near the cylinder wall two prismatic layers are applied.

The time dependent displacement of the piston, shown in Fig. 2, is conducted by a morphing motion which moves the vertices of the mesh. The morphing motion is applied to the cylinder region between 0.40D (piston at BDC) and 4.75D downstream of the piston head, and the morphing compress and expand the cells in the axial direction. For the morphed region, the cell ratio in radial direction is $D/z_{cell} = 86$, and in the axial direction the ratio is $z/D = 46$ (piston at BDC), and $D/z_{cell} = 60$ (piston at $z/D = 1.0$, standstill). Five prismatic layers are applied near the cylinder wall, with a surface averaged $y^+ < 1$.

Several earlier studies have been performed by assuming rotational symmetry and modelling the cylinder using a sector domain with cyclic boundary conditions (Carapanayotis, 1988; Sigurdsson et al., 2014). To investigate the consequences of this simplification, simulations based on a sector domain is performed. The same overall mesh strategy is used, however a refinement near the cylinder axis occurs due to the sharp edge introduced by the sector geometry. Investigations of the refinement near the cylinder axis, in the full 3D simulation, do not reveal any significant influence on velocity gradients or magnitudes (not shown). The final sector grid (12°) contains 364,000 cells, corresponding to approximately 10.9 million cells for a full 3D mesh (360°). This investigation is only carried out using the URANS turbulence model, as the symmetric boundary will suppress the resolved large scale turbulent eddies of the LES model.
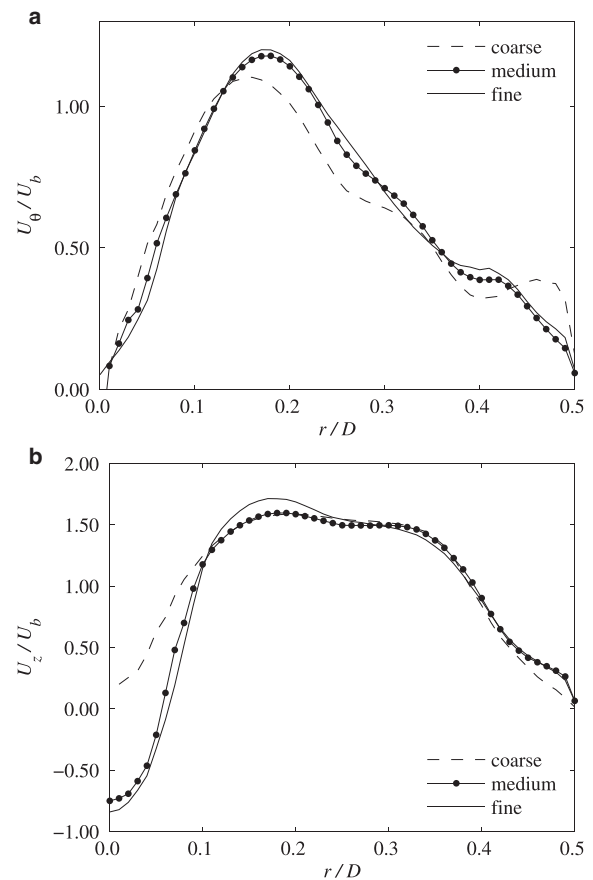

Fig. 4. Comparison of radial velocity profiles for different mesh resolutions. Results are obtained with the $k - \omega$ SST turbulence model at $z/D = 1$.

2.5. Solver

The commercial CFD code STAR-CCM+ version 8.02.008 (Limited, 2013) is used to solve the model equations. The flow equations are solved using a collocated variable arrangement and a pressure-velocity coupling of the Rhie-and-Chow-type, combined with a SIMPLE-type algorithm. The discretization scheme for the convective terms is a second-order upwind scheme for the URANS calculations and a bounded central differencing scheme for the LES calculations. The bounded central differencing scheme is a blend between the second-order upwind scheme and a central-differencing scheme. The turbulent kinetic energy is preserved with the central-differencing scheme, contrary to the upwind scheme. For the temporal discretization a second-order implicit scheme is used. To reduce the computational time, the new time step Δt_n is adjusted based on the maximum convective Courant number in the domain. The convective Courant number is defined as

$$C = \frac{\Delta t \, u_c}{\Delta x_c} \tag{10}$$

where u_c is the local velocity and Δx_c is the cell size. The upper limit of the maximum convective Courant number in the domain is defined differently for two regions in the domain. The first region is the entire computational domain, and the second region is the lower part of the cylinder ($z/D = 0.00$ to $z/D = 0.40$), with the upper limits of the maximum convective Courant numbers $C = 15.00$ and $C = 3.75$, respectively. The lower part of the cylinder is chosen to ensure a good temporal discretization of the injection process. The average convective Courant number with piston at BDC is less
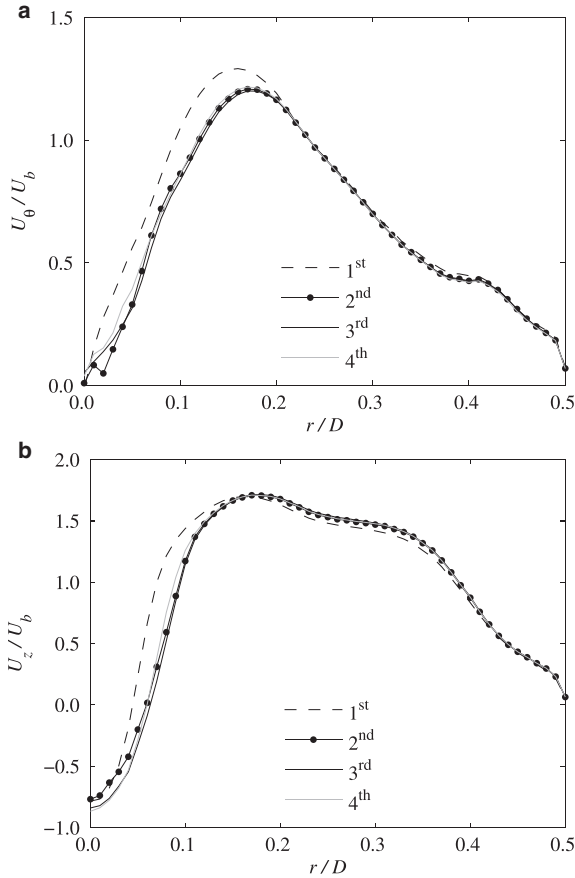
Fig. 5. Radial profiles of a) the axial and b) the tangential velocity at $z/D = 1$ for investigation of the cycle dependency. The $k - \omega$ SST model is used, and the cycle time is $t/t_{cyc} = 0.30$.

Fig. 6. Radial profiles of a) the axial and b) the tangential velocity at $z/D = 1$ for investigation of the cycle dependency. The LES WALE model is used, and the cycle time is $t/t_{cyc} = 0.32$.

than 0.20 for all the simulations. The wall clock time for one cycle running in parallel on 16 cores (dual-processor 8-core Intel Sandy Bridge Xeon E5-2650) is approximately 450 hours.
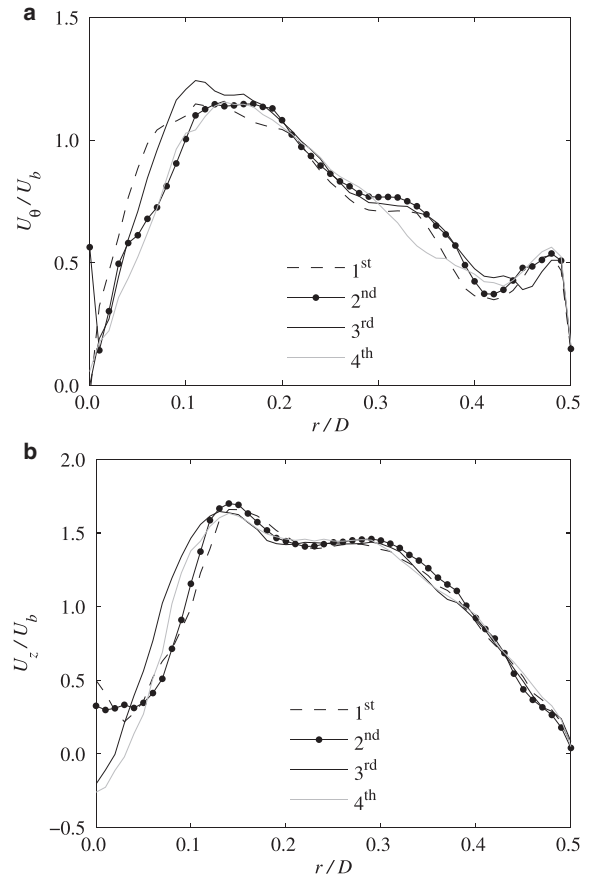
2.6. Post processing

The three-component instantaneous velocity field is sampled at the four measurement locations, $z/D = \{1.00, 2.00, 3.00, 4.00\}$ (cf. Fig. 1). The computational costs limits the data collection time to a few cycles. For representation the velocity components are transformed to cylindrical components. The coordinates of the cylindrical coordinate system is r, θ, z with the corresponding velocity components U_r, U_θ, U_z. An averaging of the velocity components in the cylindrical coordinate system is carried out converting the data into single radial profiles using the geometrical center as origin. The experimental data presented is also based on the geometrical center. The bulk velocity is found by an area average of a sectional plane at $z/D = 1.5$ for the axial velocity. Experimental bulk velocity is measured at the same location.

2.7. Sensitivity analysis

The CFD model is verified by an investigation of the sensitivity of the temporal and spatial resolution. For the URANS-based k-ω SST, three different meshes are used: the "coarse mesh", the "medium mesh", and the "fine mesh" with the respective number of cells being 1.6, 2.8, and 5.1 million.

For the LES simulations a mesh of 7.4 million cells is used. The average ratio of turbulent viscosity and molecular viscosity is 4.1 in the scavenge cylinder indicating a sufficient resolution (Davidson, 2009).

Spatial convergence of U_θ/U_b and U_z/U_b are shown in Fig. 4 using a representative axial location and scavenge time. The "coarse mesh" does not capture the deficit of the axial velocity close to the cylinder axis, cf. Fig. 4b, and it does not predict the flow reversal region. In the near wall region the axial velocity for the "coarse mesh" deviates from the "fine mesh", and the steep gradient is not predicted. The "medium mesh" and the "fine mesh" have small deviations at the velocity peak and deficit. In Fig. 4a the tangential velocity profiles are shown. The "coarse mesh" over-predicts the tangential velocity close to the wall, but underpredicts the velocity peak compared with the "fine mesh". The solution of the "fine mesh" and the "medium mesh" displays minor deviations in the tangential velocity profiles, and therefore the "fine mesh" is assumed to be a solution independent of the mesh size. In the remaining of this paper, the "fine mesh" is used for the $k - \omega$ SST model.

The radial profiles are highly dependent on the initial velocity distribution in the computational domain at the beginning of the cycle. A zero velocity field in the computational domain is set as initial condition at the beginning of the first cycle. In Fig. 5 the radial profiles are shown for four different cycles using the $k - \omega$ SST model for the "fine" mesh. It is worth noticing the large deviation from the first cycle to the remaining cycles. Both in Fig. 5a and b the second cycle slightly deviates from the third and the fourth cycle. The third and the fourth cycle obtain close to a periodic solution in the whole cycle, and for remaining of this paper the third cycle is used for presentation of results for the $k - \omega$ SST model.

LES simulations resolve the large scale fluctuations and hence require temporal averaging to produce mean quantities. In the present study, this entails a phase average of several cycles, until
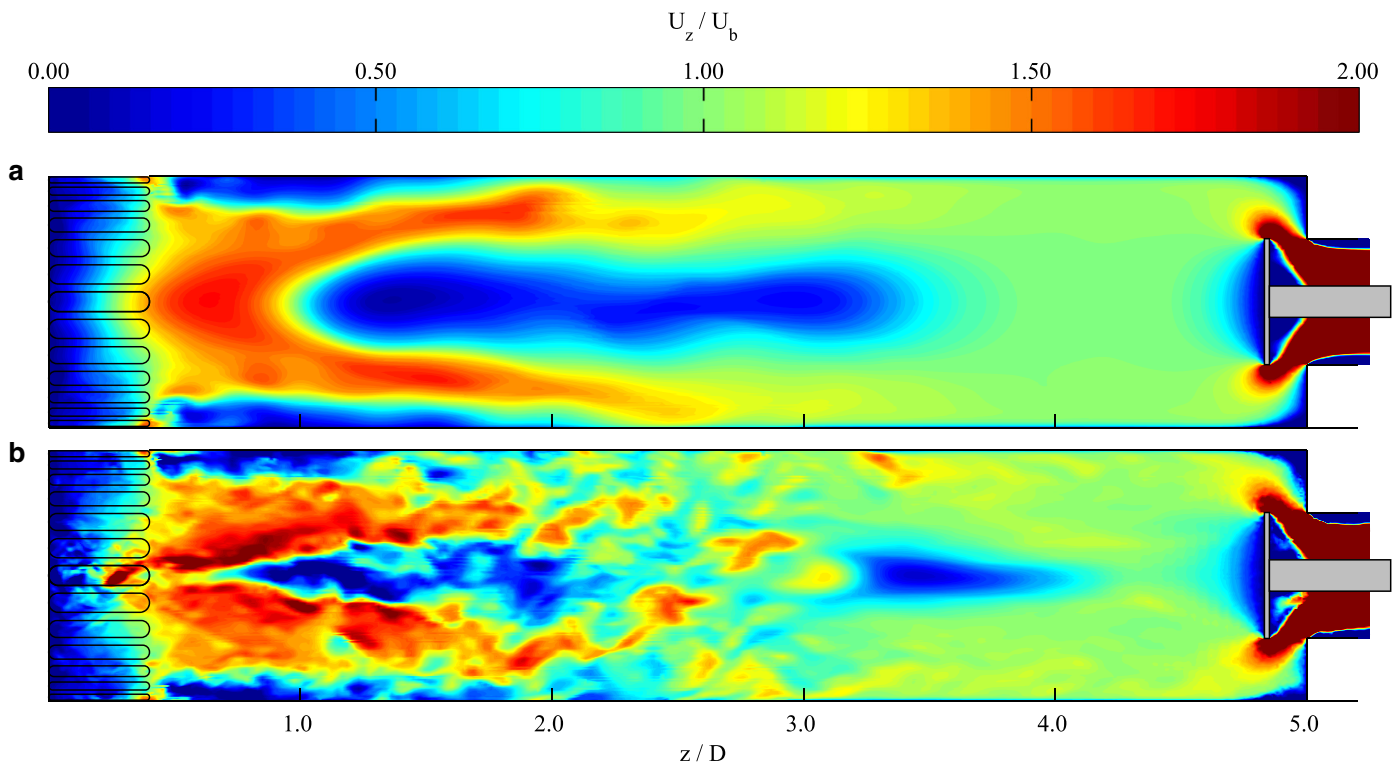
Fig. 7. A snap-shot of the axial velocities as piston has reached BDC ($t/t_{cyc} = 0.25$), is visualized using the two turbulence models a) $k - \omega$ SST and b) LES WALE. The planes lie between two scavenge ports.

converged radial profiles are obtained. However, the large computational time for one cycle, limits the number of cycles obtained in the present study. In Fig. 6 the radial velocity profiles are shown for four cycles using the LES WALE model. The velocity profiles deviate from cycle-to-cycle and does not produce a strictly periodic solution. A close study of all the radial velocity profiles at all the cycle times, indicates a quasi periodic solution from the third cycle, similar to the URANS models. In Fig. 6b the axial velocity shows deviation between the two first cycles and the two last cycles at the deficit near the cylinder axis. The bulk velocity W_b also indicates a semi periodic solution for the third and the fourth cycle (not shown). A phase-averaging using the third and the fourth cycle is carried out for the radial profiles for the LES WALE model in the remaining part of this paper.

3. Results

The instantaneous axial velocity is shown as a contour plot in Fig. 7 when the piston is at the BDC for the $k - \omega$ SST model (Fig. 7a) and the LES WALE model (Fig. 7b). Above the scavenge ports large axial velocities are present, caused by the secondary flow in the scavenge ports and near the cylinder wall between two scavenge ports. In the exhaust pipe high velocities are present, as the fluid is accelerated due to the geometrical contraction. The velocity field for the LES WALE model (cf. Fig. 7b) shows, as expected more fluctuations, and near the cylinder axis low axial velocities are seen at $z/D = 1.0$. The low axial velocity near the cylinder axis is generated by the low pressure in the swirl core. For the $k - \omega$ SST model the low axial velocity near the cylinder axis is downstream of $z/D = 1.0$ (cf. Fig. 7b), and less fluctuations are seen as we only resolve the very large eddies.

3.1. Flow rate

The bulk velocity W_b measured at $z/D = 1.5$ is shown in Fig. 8 for the $k - \omega$ SST model and the LES WALE model along

with phase-averaged LDA and phase-averaged PIV measurements (Ingvorsen et al., 2014). A good agreement between the experimental and numerical results are seen. The bulk velocity is negative when the piston is moving down and the cylinder volume is expanded. The bulk velocity is rapidly increased as the scavenge ports open and continues to increase until BDC is reached. A small delay is observed in the two numerical bulk velocities compared with both the LDA and the PIV measurements. In Fig. 8b a close up of the bulk velocity in the scavenge time, shows the difference between numerical and experimental results. From BDC to before SPC the flow rates are virtually constant only with small oscillations (cf. Fig. 8b). The oscillations are only seen in the numerical results, as the experimental data is smoothed by a phase-averaging. These oscillations are due to an internal fluctuations of the air and has a frequency that is consistent with the theoretical frequency for a stopped pipe (Ingvorsen et al., 2014; Young and Freedman, 2004). The stopped pipe is characterized by an open end and a closed end, and the frequency is defined as $f = c_{air}/(4L)$, where c_{air} is the speed of sound in air, and L is the length of the cylinder. The uncovered scavenge ports act as an open end and the cylinder head as a closed end.

3.2. Section model approximation

Modelling the engine flow using a section domain, implies simplifying the full 3D flow effects occurring in the scavenging process. Fig. 9 shows the comparison of the radial profiles using the two different modelling approaches for the $k - \omega$ SST model. The deviation is largest in the lower region of the cylinder, especially in the central region of the axial velocity, large deviations are observed. The section model predicts a flow reversal region at $t/t_{cyc} = 0.25$, where the full 3D model predicts a non-reversal flow at the cylinder axis. The sector model is in good agreement with the full 3D model for the tangential velocity, as the ports are covered, as both modelling approaches predict an identical solid body rotation. The two modelling approaches are also almost identical
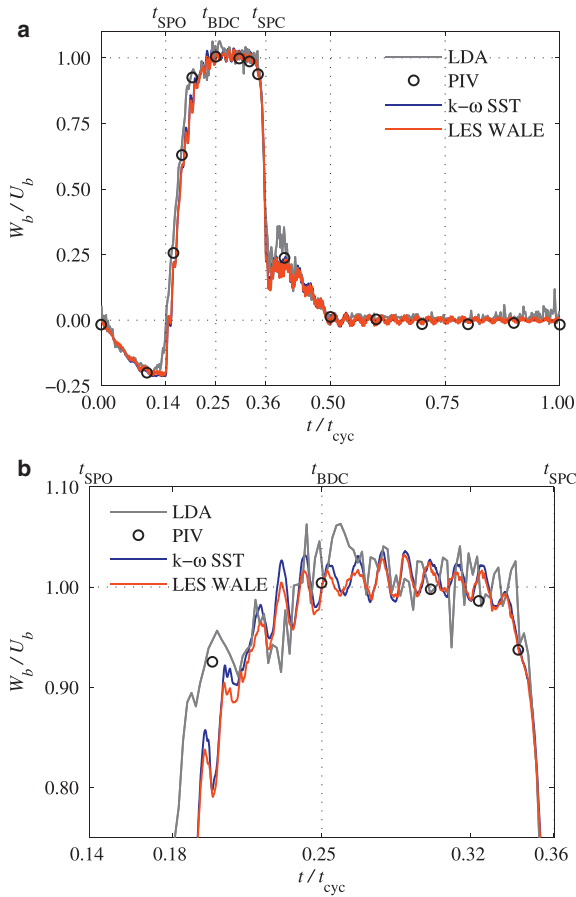
Fig. 8. Numerical and experimental normalized bulk velocity. Experimental normalized bulk velocity for the LDA and the PIV measurement (Ingvorsen et al., 2014) are phase-averaged, and measured at $z/D = 1.5$. The numerical simulations, using the $k − \omega$ SST model is for one cycle (the 3rd). a) Normalized bulk velocity over entire cycle and b) close up of the normalized bulk velocity in the scavenging period.

at $z/D = 3.0$ and $z/D = 4.0$ in the scavenge period. In the standstill period of the piston, pressure waves cause oscillations of the axial velocity. The oscillations of the axial velocity are quickly damped by the sector model compared with the damping of the oscillations for the full 3D model. An overall qualitative good agreement is seen between thesection model and full 3D model, but non-negligible differences are observed, in particular the magnitude of the backflow observed at the center of the axis.
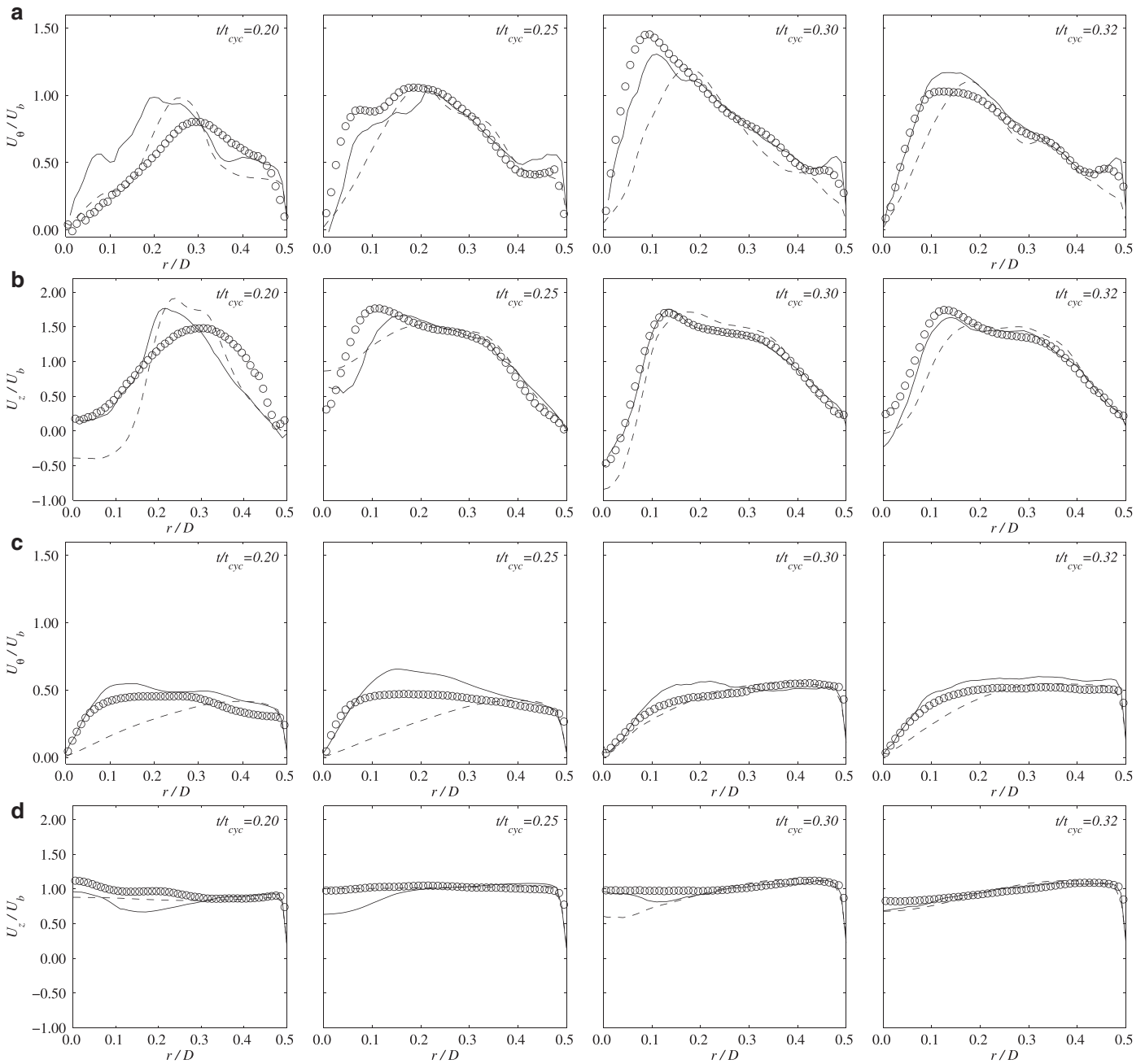
3.3. Radial profiles

We compare the accuracy of the $k − \omega$ SST and LES WALE model by considering the radial profiles of the velocity at different representative times and axial positions using the phase-averaged experimental data of Ingvorsen et al. (2014). Radial profiles of the tangential velocity (U_θ), and the axial velocity (U_z) are presented in Fig. 10.

Considering the radial profiles of the tangential velocity in Fig. 10a and c the following is pointed out. As the scavenge ports are uncovered, both turbulence models have difficulties in predicting the flow at $z/D = 1.0$. The $k − \omega$ SST model predicts the strong shear near the cylinder axis, but over- and underpredicts the tangential velocity between $r/D = 0.2$ and the cylinder wall. The prediction of the radial profiles in the opening of the scavenge ports is less accurate, compared with the closing of the ports. Large temporal variation of the radial profiles are present in both the opening and the closing, but the poor prediction of the radial profiles in the opening is speculated to be connected with a temporal delay, seen in the bulk velocity in Fig. 8. At $z/D = 4.0$ the LES model predicts the shear near the cylinder axis, whereas the $k − \omega$ SST predicts a solid body rotation. The solid body rotation is seen for the different URANS based models in preliminary simulations (not shown), whereas the LES model correctly predicts the shear near the cylinder axis present in the experimental data. As the piston is stationary at $z/D = 1.0$ the general picture of the URANS model is a solid body rotation, whereas the LES model predicts a non-solid rotation. As the piston reaches the BDC, the radial profiles are slightly underpredicted by the LES WALE model at $z/D = 1.0$. The $k − \omega$ SST
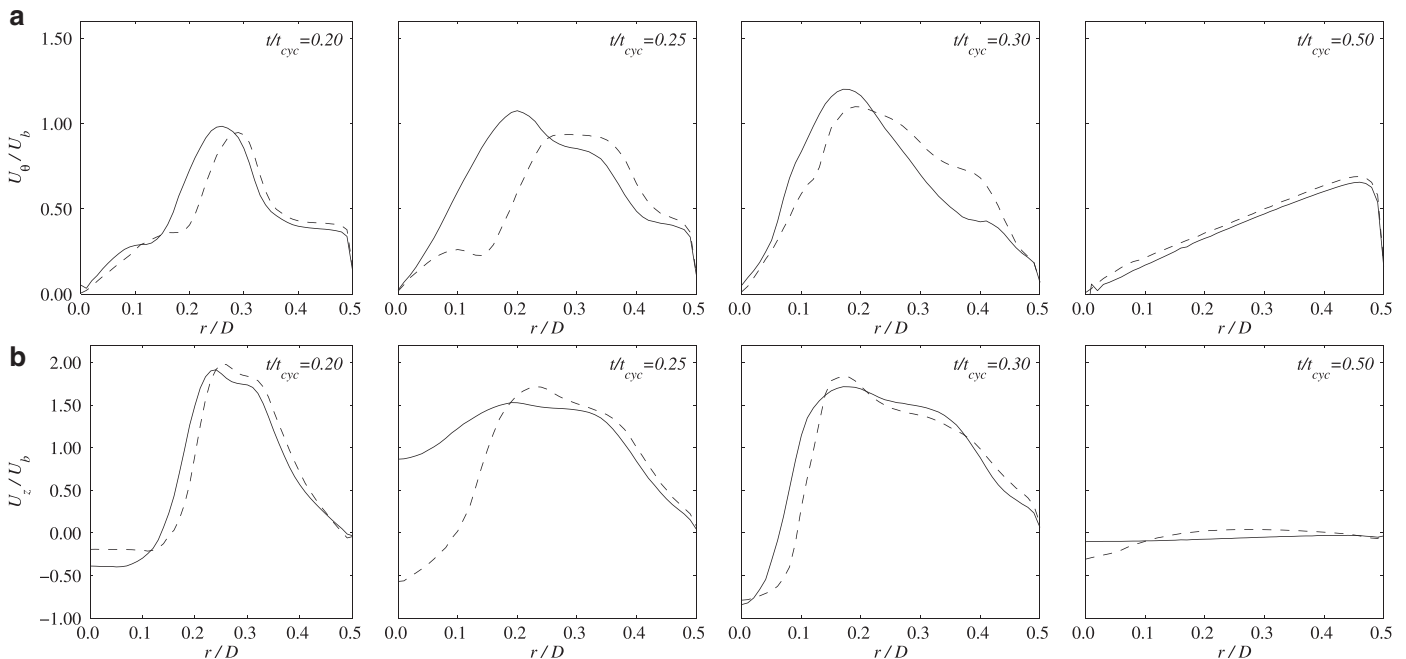
Fig. 9. Radial profiles of a) the tangential velocity and b) the axial velocity at different representative times. *Solid line*: the full 3D modelling and *dashed line*: the sector modelling. The $k − \omega$ SST model is used as the turbulence model for both approaches. The axial location is $z/D = 1.0$ for $t/t_{cyc} = \{0.20, 0.25, 0.32\}$ and $z/D = 2.0$ for $t/t_{cyc} = 0.50$.

Fig. 10. Radial profiles of (a,c) the axial and (b,d) the tangential velocity, in 3rd cycle. Four different scavenge times, $t/t_{cyc} = \{0.20, 0.25, 0.30, 0.32\}$ starting from the left and two different axial locations (a,b) $z/D = 1.00$, c),d) $z/D = 4.00$. *Open circles*: experimental data, *dashed line*: $k - \omega$ SST model, *solid line*: LES WALE model.

model has difficulties in predicting the tangential profile near the cylinder axis, but a good agreement is seen in the outer region. At $z/D = 4.0$ both models are in good agreement with the experimental data in the outer region. The LES WALE predicts the gradient near the cylinder axis, but overestimate the profile in the central part of the radial profile. The $k - \omega$ SST predicts a solid body rotation and underpredicts the profile. As the piston start to cover the ports the models are in good agreement with the experimental, except for the $k - \omega$ SST near the cylinder axis at $z/D = 1.0$.

Now considering the radial profiles of the axial velocity in Fig. 8b and d the following is noted. The turbulence models has difficulties in capturing the axial velocity as the ports open at $z/D = 1.0$ as for the tangential velocity. As the piston reach the BDC and begins the covering of the scavenge ports a good agreement is seen at $z/D = 1.0$, especially for the LES WALE model. At

$z/D = 4.0$ the outer regions of the profiles are in good agreement with the experimental data, but both models tends to underestimate the axial velocity in the center.

The integrated relative error from the experimental data for the whole cycle is shown in Fig. 11. The percentage deviation is based on U_b and it is the average error of the four different axial locations, i.e. $z/D = \{1.0, 2.0, 3.0, 4.0\}$. It should be noted that the percentage deviation is an approximate measure of the model accuracy, as it is based on the velocity difference at different radial positions. The LES WALE model predicts the axial velocity, cf. Fig. 11b, with good agreement between the fully open ports and the 75% covered ports. In this time interval the bulk velocity is approximately constant and the temporal gradients are small. The LES WALE model is the poorest model to predict the tangential velocity in the stationary part of the cycle. This is connected with a
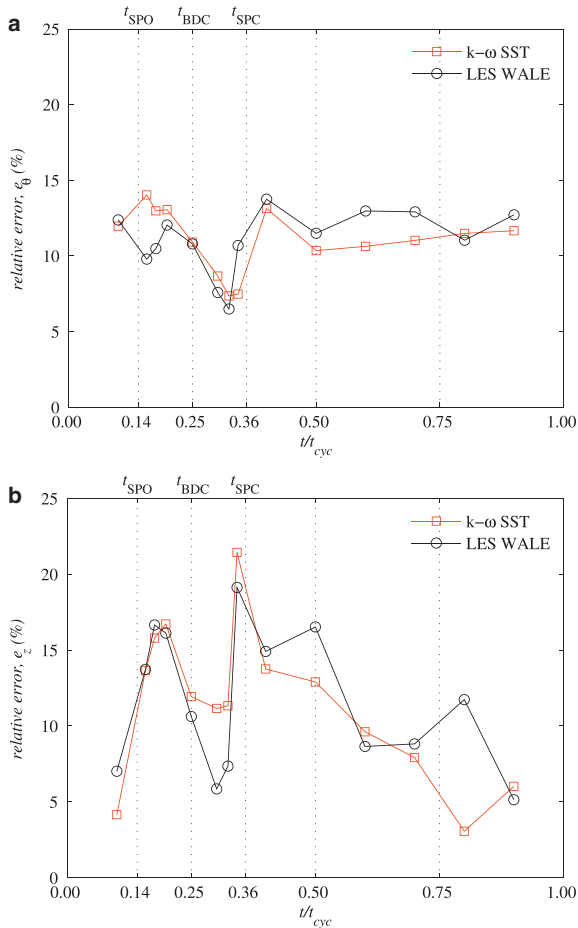
Fig. 11. The relative error for the different turbulence models. The relative error is estimated as $e_i = |U_{i,num} - U_{i,exp}|/U_b$. a) the tangential and b) the axial relative error.

general overestimation of the tangential velocity in the central part of the radial profiles. The average deviation for the whole cycle is 11% for both turbulence models.

3.4. Coherent structures

Using proper orthogonal decomposition (POD) analysis of the velocity field, Ingvorsen et al. (2014) experimentally investigated the flow at $z/D = 1.0$ for the times $t/t_{cyc} = \{0.25, 0.30\}$. The investigation showed the presence of two mode pair for the time $t/t_{cyc} = 0.30$, where the first mode pair corresponds to a displacement of the vortex core, and the second to an in-plane deformation of the vortex core or the formation of two separate swirl centers. At the time $t/t_{cyc} = 0.25$ only the first mode pair is observed.

In Fig. 12 the swirl centers at different times are visualized for the LES model by an isosurface of the pressure, along with an isosurface of the flow reversal region ($U_z/U_b = 0.0$). The investigated region is limited to the vortex breakdown that lies in the spatial range $0.0 < z/D < 2.0$ and $0.0 < r/D < D/4$. The flow is observed to possess a precessing vortex core (PVC) (Alekseenko et al., 1999) around the geometric axis of the cylinder. Furthermore, the PVC lies at the boundary between the positive and negative axial velocity and twisted opposite of the main swirl direction. At $t/t_{cyc} = 0.18$ a vortex breakdown region is observed, and a close investigation of the pressure reveals both triple- and quadruple helical structures in the region. At $t/t_{cyc} = 0.20$ the vortex breakdown region is extended downstream and a double helical structure is seen upstream of $z/D = 1.0$. As the piston reaches the BDC at $t/t_{cyc} = 0.25$ the flow reversal region is not present, and a single displaced vortex core is observed similar to the experimental data (Ingvorsen et al., 2014). The vortex breakdown region is formed again at $t/t_{cyc} = 0.30$, and a double helical structure is identified consistent with the experimental data. At $t/t_{cyc} = 0.32$ a double helical structure is observed along with a flow reversal region. One should notice that the radial profile for the experimental data of the axial velocity at $z/D = 1.0$, cf. Fig. 10b, does not show a flow reversal region at the cylinder axis.
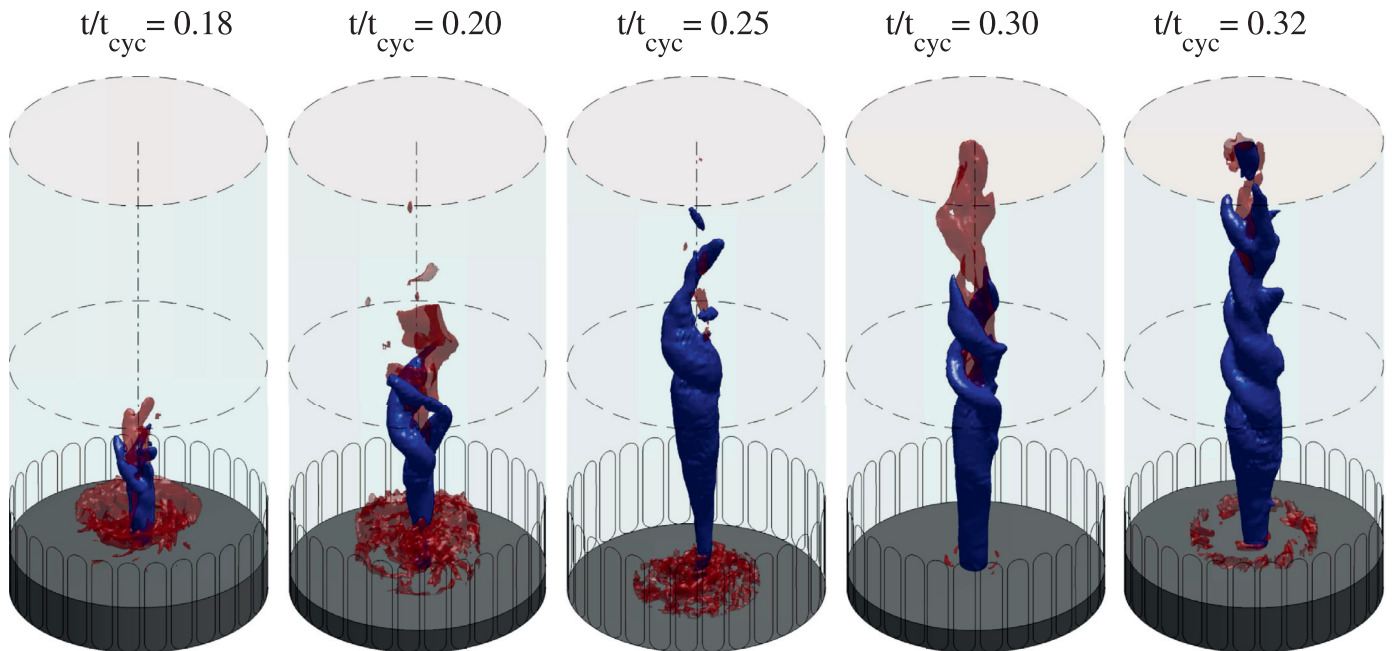
Fig. 12. Iso-surfaces of the pressure (blue color) and the axial velocity (red color). The isosurfaces are only visualized in the axial direction $0.0 < z/D < 2.0$, and in the radial direction $0 < r/D < D/4$. The isovalue of the pressure is $P/(\frac{1}{2}\rho U_b^2) = \{-6.6, -6.0, -6.0, -7.1, -7.5\}$ for the corresponding times $t/t_{cyc} = \{0.18, 0.20, 0.25, 0.30, 0.32\}$. The isovalue for the axial velocity is $U_z/U_b = 0.0$.
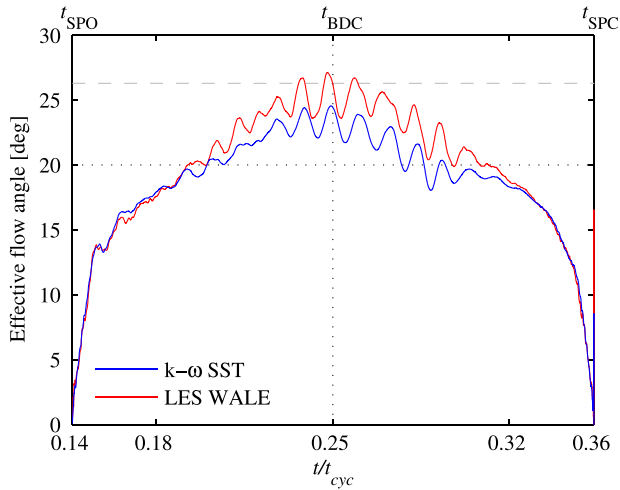
Fig. 13. Comparing the effective flow angle, based on a mass flow average, for the $k - \omega$ SST, and the LES model during the scavenge period. Geometrical angle and BDC is indicated with dotted line. The dashed line indicates the effective flow angle for the steady-flow configuration.

In the scavenging period also vortex rings are observed (not shown). Several vortex rings are shed from the top of the scavenge ports, the sharp edge on the periphery of the piston surface, and the exhaust valve.

3.5. Scavenge ports

The design of the scavenge ports influences the swirl strength in the cylinder. An experimental study (Rizk, 1958) indicated that the injected fluid, from the scavenge ports, did not match the actual geometrical angle of the scavenge ports. In this study the effective flow angle, a measure of the actual angle of injection, into the cylinder were commented based on observations. It was noticed that the flow is injected radially at the beginning of the scavenge period, and the effective flow angle increases until swirl is developed in the cylinder. Preliminary numerical investigations (not shown) of the same experimental set-up using a fixed piston shows an effective flow angle, based on a mass flow averaging, with a 31.5% higher angle compared to the angle of the scavenge ports. The investigation also investigated the flow in the scavenge ports, both numerically and experimentally. Large axial velocities are seen in a separated flow region in the scavenge ports.

The effective flow angle and the port flow are investigated through the scavenge period. The effective flow angle α_f is illustrated in Fig. 13 for both turbulence models, where $\alpha_f = \tan^{-1}(U_\theta/U_r)$. The U_r and U_θ are measured as an average value at the interface between the scavenge ports and the cylinder volume. The flow is injected radially into the cylinder as the scavenge ports are uncovered, and the flow angle increases rapidly up to $\alpha_f = 13°$. The flow angle still increases linearly but with a lower slope until the BDC ($t/t_{cyc} = 0.36$). At the BDC the two models predict different effective flow angles into the cylinder. The $k - \omega$ SST model finds a flow angle lower than the LES WALE model, and the LES WALE model predicts a similar flow angle compared with the steady-flow case. The LES WALE model therefore deliver more angular momentum to the in-cylinder swirl in the scavenge period, compared to the $k - \omega$ SST model. The frequency of the oscillations seen in the flow angle is similar to the frequency found in Section 3.1, generated by the pressure waves in the cylinder. The flow angle decreases after the BDC, and at port closure the flow angle is radial, which is different from previous observations (Rizk, 1958).

In Fig. 14 the streamlines for the spatial averaged velocity in the scavenge ports are illustrated for a plane section at $z/D = 0.3$,
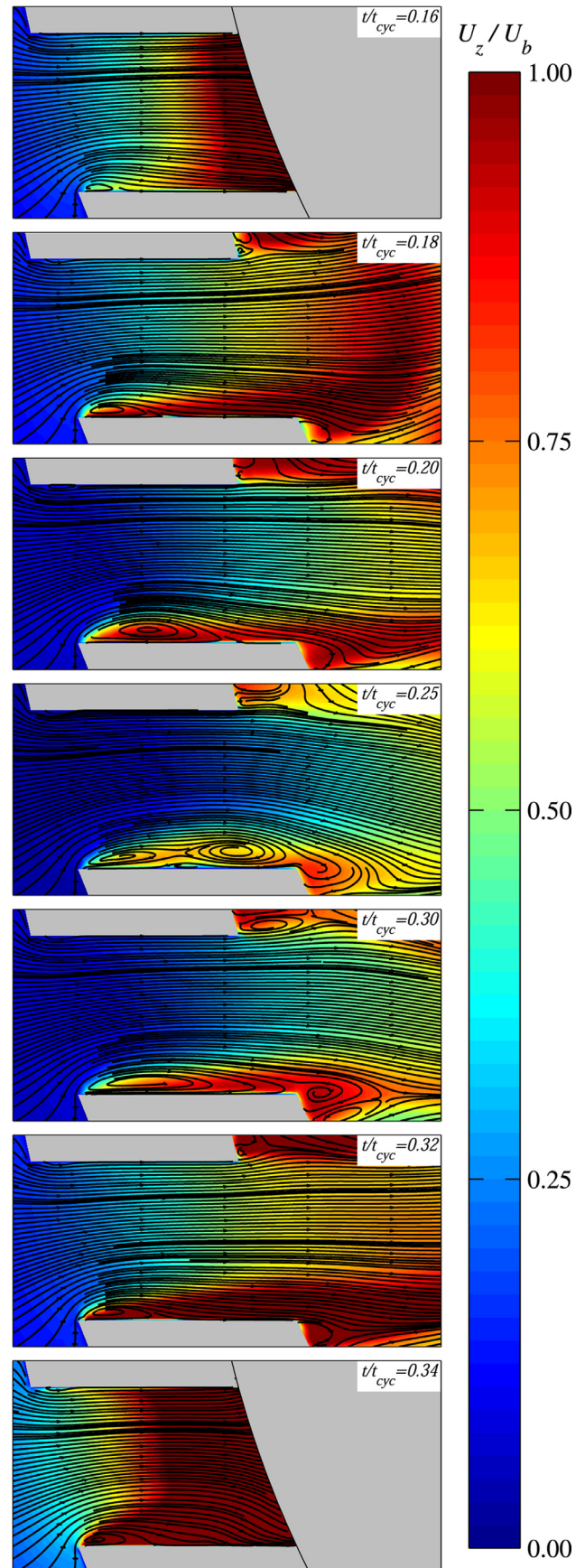
Fig. 14. Plane section at $z/D = 3.0$ showing a colour contour of the spatial averaged axial velocity inside the scavenge port using the $k - \omega$ SST model.

along with a colour contour of the spatial averaged axial velocity for different times. The spatial average is obtained by splitting each port into sections of 12° and computing an average velocity field based on the flow in the thirty ports. At $t/t_{cyc} = 0.16$ high axial velocities are seen near the piston. The flow is forced upward, from the lower part of the port and into the cylinder. At $t/t_{cyc} = 0.20$ high axial velocities are seen inside the port. The axial velocity is a secondary flow in a flow-separated region near the wall. A secondary flow in a separated flow is also present in the cylinder, between two scavenge ports. At $t/t_{cyc} = 0.34$, corresponding to 75% closed ports, the high axial velocity is present across the scavenge port. The flow is still separated near the scavenge wall, and the high axial velocity near the wall is present up to the entrance to the scavenge port. Compared with the time $t/t_{cyc} = 0.16$ more air is forced up from the lower part of the scavenge port. The secondary axial flow introduces large shear stresses on the cylinder wall, above the scavenge ports. The high wall shear stresses is expected to enhance a more effective cooling above the ports, in the case of a real engine.

4. Conclusions

The swirling flow in a dynamic model of a uniflow-scavenged cylinder has been investigated numerically. Radial profiles of the velocity are compared with experimental data for two different turbulence models, along with an investigation of the in-cylinder flow. The main conclusions of the study are:

- The $k - \omega$ SST model and the large-eddy simulation model (using the wall-adaptive local eddy-viscosity subgrid-scale model) are validated with experimental data. For both investigated turbulence models the deviation from the experimental data, based on radial profiles of the tangential and axial velocity at four axial locations, is found to be less than 11%.
- Pressure waves in the cylinder are in good agreement with theoretical predictions and experimental data.
- Comparison of the radial profiles between a full 3D simulation and a sector (12°) simulation, shows a difference due to the present of 3D structures in the scavenging process.
- Coherent structures in several vortex breakdown regions are visualized, and a good agreement with the experimental data is found.
- A secondary axial flow in a flow-separated region within the scavenge ports is identified, and it is found that the secondary flow exits the scavenge ports in the top of the port. The exit of the flow in the top of the scavenge ports introduces high wall shear-stresses on the cylinder wall above the scavenge ports.
- The effective flow angle is investigated, and it is shown that the angle is higher compared with the geometrical angle of the scavenge ports. The LES WALE model predicts a larger effective flow angle around bottom dead center compared to the $k - \omega$ SST model. This results in injection of more angular momentum for the LES model.

Acknowledgment

References

Al-Mousawi, N.M.J.K., 2012. Numerical Simulation of Swirling Flow in a Model Diesel Engine using RANS and LES Turbulence Models. Technical University of Denmark Master's thesis.

Alekseenko, S.V., Koubin, P.A., Okulov, V.L., Shtork, S.I., 1999. Helical vortices in swirl flow. J. Fluid Mech. 382, 195–243.

Carapanayotis, A., 1988. Mathematical modeling of the scavenging process in a two-stroke diesel engine. J. Eng. Gas Turbines Power 110, 538–546.

de Castro Gouveia, M., dos Reis Parise, J.A., Nieckele, A.O., 1992. Numerical simulation of the fluid flow and heat transfer processes during scavenging in two-stroke engine under steady-state conditions. J. Heat Transfer 114, 383–393.

Davidson, L., 2009. Large eddy simulations: how to evaluate resolution. Int. J. Heat Fluid Flow 30, 1016–1025.

Diwakar, R., 1987. Three-dimensional modeling of the in-cylinder gas exchange processes in a uniflow-scavenged two-stroke engine. SAE Tech. Paper Ser.. Paper No. 870596

Goldsborough, S.S., Blarigan, P.V., 2003. Optimizing the scavenging system for a two-stroke cycle, free piston engine for high efficiency and low emissions: a computational approach. SAE Tech. Paper Ser. 1, 1–22.

Haider, S., Schnipper, T., Obeidat, A., Meyer, K.E., Okulov, V.L., Mayer, S., Walther, J.H., 2013. PIV Study of the effect of piston position on the in-cylinder swirling flow during the scavenging process in large two-stroke marine diesel engines. J. Mar. Sci. Tech. 18, 133–143. doi:10.1007/s00773-012-0192-z.

Hoekstra, A.J., Derksen, J.J., Van Den Akker, H.E.A., 1999. An experimental and numerical study of turbulent swirling flow in gas cyclones. Chem. Eng. Sci. 54, 2055–2065.

Hori, H., 2000. Scavenging flow optimization of two-stroke diesel engine by use of CFD. SAE Trans. 2000-01-0903, 1–16.

Hult, J., Mayer, S., 2013. A methodology for laser diagnostics in large-bore marine two-stroke diesel engines. Meas. Sci. Technol. 24 (4), 1–10.

Ingvorsen, K.M., Meyer, K.E., Walther, J.H., Mayer, S., 2013. Turbulent swirling flow in a model of a uniflow-scavenged two-stroke engine. Exp. Fluids 54 (3), 1494.

Ingvorsen, K.M., Meyer, K.E., Walther, J.H., Mayer, S., 2014. Turbulent swirling flow in a dynamic model of a uniflow-scavenged two-stroke engine. Exp. Fluids 55, 1748.

Lamas, M.I., Vidal, C.G.R., 2012. Computational fluid dynamics analysis of the scavenging process in the MAN b&w 7S50mc two-stroke marine diesel engine. J. Ship. Res. 56 (3), 154–161.

Limited, C. D., 2013. STAR-CCM+ Version 8.02 Documentation.

Menter, F.R., 1994. Two-equation eddy-viscosity turbulence modeling for engineering applications. AIAA J. 32 (8), 1598–1605.

Moulinec, C., Benhamadouche, S., Laurence, D., Peéric, M., 2005. Les in a u-bend pipe meshed by polyhedral cells. Eng. Turb. Model. Exp. 6, 237–246.

Najafi, A.F., Saidi, M.H., Sadeghipour, M.S., Souhar, M., 2005. Numerical analysis of turbulent swirling decay pipe flow. Int. Com. Heat and Mass Trans. 32 (5), 627–638.

Nakagawa, H., Kato, S., Tateishi, M., Adachi, T., Tsujimura, H., Nakashima, M., 1990. Airflow in the cylinder of a 2-stoke cycle uniflow scavenging diesel engine during compression stroke. Jpn. Soc. Mech. Eng. 33 (3), 591–598.

Nicoud, F., Ducros, F., 1999. Subgrid-scale stress modelling based on the square of the velocity gradient tensor. Flow, Turbul. Combust. 62, 183–200.

Obeidat, A., Schnipper, T., Ingvorsen, K.M., Haider, S., Meyer, K.E., Mayer, S., Walther, J.H., 2014. Large eddy simulations of the influence of piston position on the swirling flow in a model two-stroke diesel engine. Int. J. Num. Meth. Heat Fluid Flow 24 (2), 325–341.

Percival, W.H., 1955. Method of scavenging analysis for 2-stroke-cycle diesel cylinders. SAE Trans. 63, 737–751.

Ravi, M.R., Marathe, A.G., 1992. Effect of inlet and exhaust pressures on the scavenging characteristics of a carbureted uniflow scavenged engine. SAE Tech. Paper Ser. 237–250.

Rizk, W., 1958. Experimental studies of mixing processes and flow configurations in two-cycle engine scavenging. Proc. Inst. Mech. Eng. 172 (10), 417–427.

Sher, E., Hossain, I., Zhang, Q., Winterbone, D.E., 1991. Calculation and measurements in the cylinder of a two-stroke uniflow-scavenged engine under steady flow conditions. Exp. Therm. Fluid Sci. 4, 418–431.

Sigurdsson, E., Ingvorsen, K.M., Jensen, M.V., Mayer, S., Matlok, S., Walther, J.H., 2014. Numerical analysis of scavenge flow and convective heat transfer in large two-stroke marine diesel engines. Appl. Energy 123, 37–46.

Sung, N.W., Patterson, D.J., 1982. Air motion in a two stroke engine cylinder − the effects of exhaust geometry. SAE Trans. 2534–2544. Paper No. 820751

Uzkan, T., 1988. The effects of engine speed on the scavenging characteristics of a two-cycle engine. J. Eng. Gas Turbines Power 110, 523–530.

Wilcox, D.C., 1994. Turbulence Modeling for CFD. DCW Industries, Inc..

Young, H.D., Freedman, R.A., 2004. Sears and Zemansky's University Physics: With Modern Physics. Addison-Wesley Publishing Company.

Yuan, S.P., So, R.M.C., 1998. Turbulent rotating flow calculations: an assessment of two-equation anisotropic and reynolds stress models. Proc. Inst. Mech. Eng. G. - J. Aer. 212, 193–212.